Angewandte Chemie
Eine Zeitschrift der Gesellschaft Deutscher Chemiker

Supporting Information

Photoproduction of Hydrogen by Decamethylruthenocene Combined with Electrochemical Recycling

Lucie Rivier, Pekka Peljo, Laurent A. C. Vannay, Grégoire C. Gschwend, Manuel A. Méndez, Clémence Corminboeuf, Micheál D. Scanlon, and Hubert H. Girault**

anie_201610240_sm_miscellaneous_information.pdf

Table of Contents

Section 1: Materials and experimental techniques.

Reagents. All chemicals were used as received without further purification. All aqueous solutions were prepared with ultrapure water (Millipore Milli-Q, specific resistivity 18.2 MΩ·cm). The solvents used were 1,2-dichloroethane (DCE, ≥99.8%, Fluka), deuterated dichloromethane (CD_2Cl_2, 99.8+ atom% D, Merck), ethanol (≥98.8%, Sigma-Aldrich), hydrochloric acid (HCl, 37%, Merck) and sulfuric acid (H_2SO_4, 95-97%, Merck). Decamethylruthenocene ($Cp_2^*Ru^{(II)}$, 99%) and decamethylferrocene ($Cp_2^*Fe^{(II)}$, 99%) was supplied by ABCR and stored in a N_2-filled glove-box until use. Tetrabutylammonium hexafluorophosphate ($TBAPF_6$, ≥99.0%) was obtained from Sigma-Aldrich. Bis(triphenylphosphoranylidene)ammonium chloride (BACl, 98%) and potassium hydrohyde (KOH, 85%) were purchased from Fluka. Lithium tetrakis-(pentafluorophenyl)borate ethyl etherate ($Li(OEt_2)_2$]TB purum) was purchased from Boulder Scientific. Bis(triphenyl-phosphoranylidene) ammonium tetrakis(penta-fluorophenyl)borate (BATB) was prepared by metathesis, as described previously.[1]

Preparation of tetrakis(pentafluorophenyl)borate diethyl etherate acid ([$H(OEt_2)_2$]TB). 2 g of [$Li(OEt_2)_2$]TB was dissolved in 30 mL of 6 M HCl (Acros) to prepare [$H(OEt_2)_2$]TB. To ensure that the $H(OEt_2)^{2+}$ cation was formed a few mLs of ether were added to this mixture. The latter is a critical step in the synthesis as the non-etherated version of this acid, [H]TB, although predicted to be an exceptionally strong acid,[2] cannot be synthesised as the TB^- is unstable with respect to B-phenyl bond cleavage.[3] The diethyl etherate prepared here is a weaker acid than the theoretical non-etherated [H]TB but much more stable.[4] Next, [$H(OEt_2)_2$]TB was extracted by addition of DCM (30 mL) and the aqueous layer was further washed with DCM (2 × 15 mL) after phase separation. The combined organic layers were dried over sodium sulfate (Na_2SO_4, Reactolab). Finally, Na_2SO_4 was removed by filtration and DCM evaporated under reduced pressure to yield the organic soluble acid [$H(OEt_2)_2$]TB as a white powder.

^{1}H NMR spectroscopy. All NMR analysis were performed on a Bruker Biospin Avance-400 spectrometer. Chemical shifts are expressed in parts per million (ppm) relative to CD_2Cl_2 (δ = 5.32 ppm).[5] DCE was used as an internal standard and added at a concentration of 31.2 mM.

Electrochemical experiments. Cyclic voltammetry (CV) and chronoamperometry experiments were performed in a three-electrode configuration using a PGSTAT 30 potentiostat (Metrohm, CH) under anaerobic conditions in a N_2-filled glove-box and at ambient temperature. A fluorinated tin oxide (FTO) working electrode (15 Ω per sq, 2.2 mm thickness, Solaronix) was contacted with a de-oxygenated solution of DCE containing 0.1 M $TBAPF_6$ as supporting electrolyte. CVs were obtained in a glovebox under anaerobic conditions at ambient temperature using a platinum (Pt) wire (for electrochemical measurements) or Pt disk (2 mm Ø, for gas measurements) as the counter electrode. The reference electrode used for measurements in organic media was a double-junction reference electrode encompassing a Pt wire. The inner and outer chambers contained a Pt wire in a solution of 0.1 M $TBAPF_6$ in acetonitrile and were separated by a porous silica bead, replacing the typically used Vycor(R) porous glass frit. CVs were calibrated *versus* the formal reduction potential of $Cp_2^*Fe^{(II)}$ in DCE on the standard hydrogen electrode (SHE) scale ($[E^{0\prime}_{[Cp_2Fe(III)]^+/Cp_2Fe(III)}]^{DCE}$ = 0.07 V *vs.* SHE).[6] For the controlled potential electrolysis (CPE) experiments, a potential of 0.50 V *vs.* SHE was applied, *i.e.,* a sufficiently negative potential to regenerate $[Cp_2*Ru^{(III)}]^+$ but not so negative as to spontaneously evolve H_2 on the FTO electrode surface in the dark. Illumination of the electrochemical cell was possible using a 365 nm LED (Thorlabs, M365L2) through the FTO electrode.

FTO electrode washing. FTO plates were immersed in 4.7% KOH in ethanol/water (4:1) and sonicated for 5 minutes. Then, the plates were washed with water and immersed in 0.1 M H_2SO_4. Subsequently, they were washed a second time with water and finally dried.

UV/vis spectroscopy. An Ocean Optics USB 2000+ fiber optic spectrophotometer was employed for kinetics experiments. All other UV/vis analysis, including spectroelectrochemical analysis (discussed *vide infra*), was performed on an Agilent Carry 8453 photodiode array spectrophotometer.

Spectroelectrochemistry experiments. A 6 mM solution of $Cp_2^*Ru^{(II)}$ in DCE with 20 mM BATB as supporting electrolyte, was placed in a thin-layer quartz cuvette. The cell configuration was composed of a Pt mini-grid as the working electrode, a Pt wire as the counter electrode and reference electrode described above. The solution was oxidized using

chronoamperometry for 120 s at a series of applied potentials spaced at regular intervals between 0.22 and 0.91 V (*vs.* SHE). The response was followed by UV/vis spectroscopy.

Laser specifications. Ekspla PL2230 Series combined with a Ekspla PG400 Series OPG.

Gas chromatography (GC). 1 mL samples of the headspace gas were obtained by using a lock-in syringe with a push–pull valve (SGE Analytical Sciences) and subsequently analyzed by a PerkinElmer gas chromatograph (Thermo Scientific Trace 1300, equipped with a 20 mL loop, HAYESEP DB and an 100/120 mesh) with a thermal conductivity detector (TCD) and argon as the carrier gas. For long experiments, DCE tends to evaporate. Therefore, at the end of the reaction, the solution was collected and weighed to calculate the remaining volume of DCE. This was in order to precisely evaluate the volume of the headspace and determine the amount of H_2 produced from the concentration of H_2 given by GC.

Section 2: Spectroscopic studies monitoring hydride formation (conversion of $Cp_2^*Ru^{(II)}$ to $[Cp_2^*Ru^{(IV)}(H)]^+$).

^1H NMR spectra shown in Figure S1 were obtained in deuterated dichloromethane (CD_2Cl_2) using DCE (31.2 mM) as an internal standard, in the dark, at ambient temperature and under anaerobic conditions. The similarities of the two solvents, CD_2Cl_2 and DCE, in terms of being weakly coordinating, having similar dielectric constants, *etc.* were such that the trends seen by NMR in CD_2Cl_2 were expected to accurately reflect the processes that occur in DCE under otherwise identical experimental conditions. Firstly, the ^1H NMR spectrum of pristine $Cp_2*Ru^{(II)}$ was obtained prior to the addition of organic acid, see Figure S1A. All of the protons of the methyl groups on each cyclopentadienyl ring for $Cp_2*Ru^{(II)}$ are chemically equivalent, showing a characteristic singlet chemical shift (δ) at 1.62 ppm, in agreement with previous studies.[7] The ^1H NMR spectrum of $[Cp_2*Ru^{(IV)}(H)]^+$, formed *in situ* by reaction with an excess of 1.3 equivalents of the strong Brønsted acid $[H(OEt_2)_2]TB$, showed a singlet peak at –8.38 ppm corresponding to the hydridic Ru–H proton, see Figure S1B. In addition, the signal for the protons of the methyl groups on each cyclopentadienyl ring was shifted positively to 1.83 ppm. The latter was due to the reduced electron density on the cyclopentadienyl rings to compensate the Ru oxidation, leading to the slight de-shielding of the protons of the methyl groups. This initial protonation step is in agreement with the mechanism of H_2 evolution expected from metallocenes, whether light-activated or not.[7a]

Spectroscopic characterization of the conversion of $Cp_2^*Ru^{(II)}$ to $[Cp_2^*Ru^{(IV)}(H)]^+$ with $[H(OEt_2)_2]TB$ organic acid illustrated in Figure S3(A) showed the appearance of a main absorption band at 243 nm as well as a broad absorption in the near-UV. However, no isobestic point was observed due to the absorption of $[H(OEt_2)_2]TB$ in this region (see Figure S4). To confirm the formation of $[Cp_2^*Ru^{(IV)}(H)]^+$ as a unique product, the titration was repeated with CF_3SO_3H which does not absorb in UV (see Figure S3(B)). In this case, a clear isobestic point was observed at 231 nm. The main absorption band did not shift as function of the counter ion of the acid and was still observed at 243 nm.

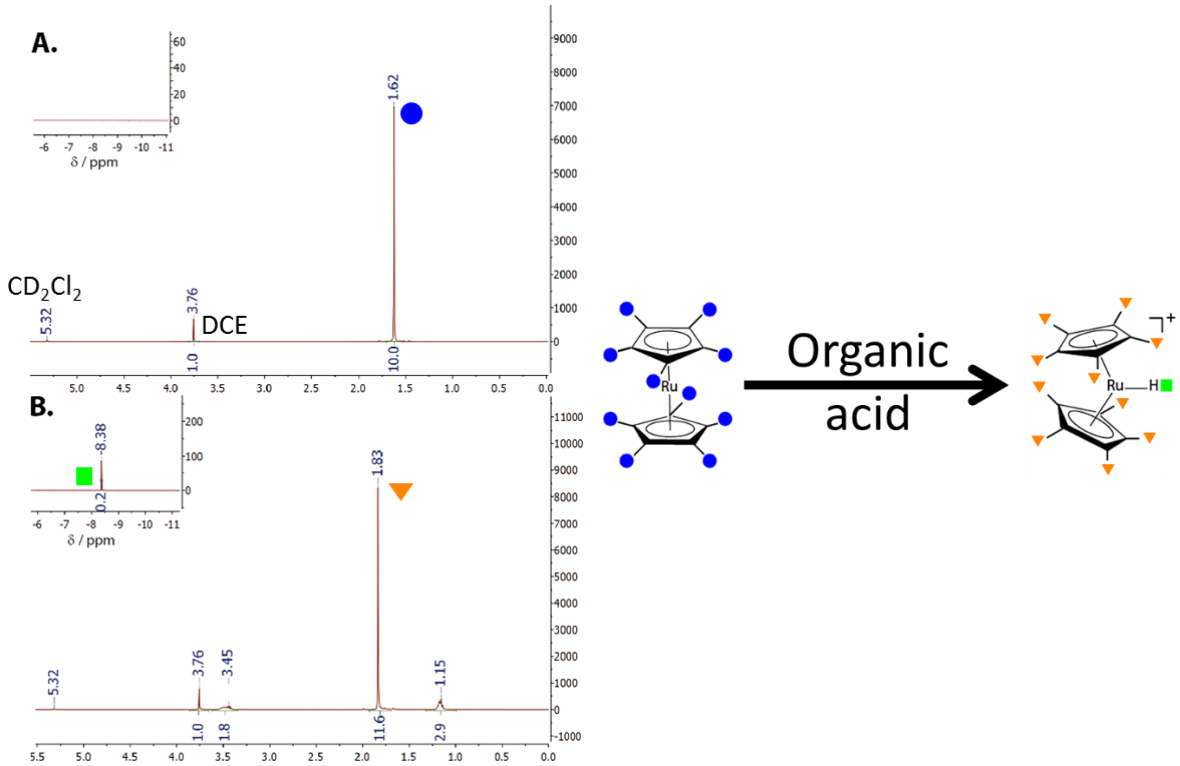

Figure S1. ^{1}H NMR spectra of **(A)** 15 mM $Cp_2^{*}Ru^{(II)}$ and **(B)** 15 mM $[Cp_2^{*}Ru^{(IV)}(H)]^{+}$, generated by reacting 15 mM $Cp_2^{*}Ru^{(II)}$ with 20 mM HTB**.** ^{1}H NMR spectra were obtained in deuterated dichloromethane (CD_2Cl_2) solvent using DCE (31.2 mM) as an internal standard, in the dark, at ambient temperatures and under anaerobic conditions.

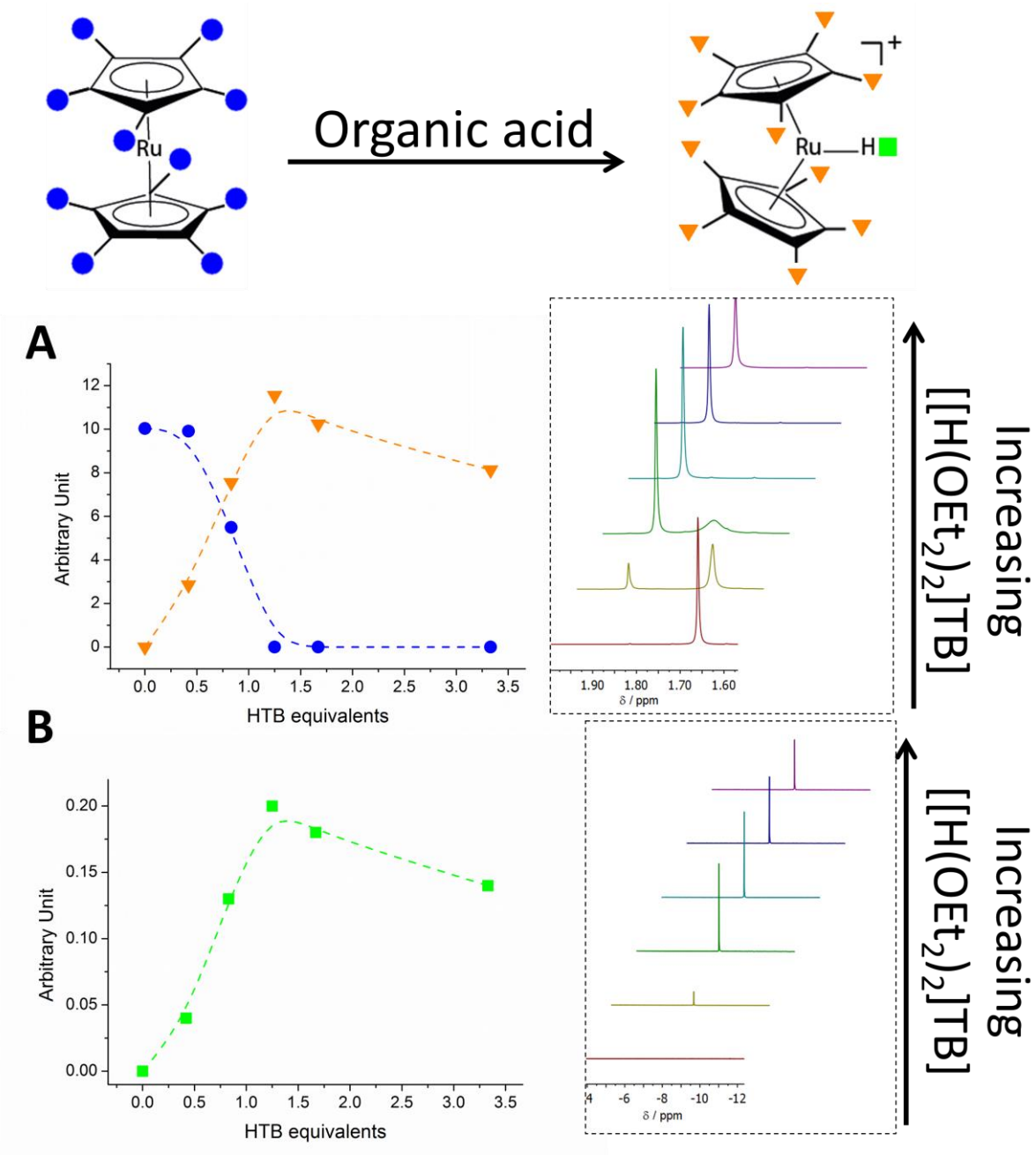

Figure S2. Metal hydride formation followed by ^{1}H NMR in the presence of [H(OEt$_2$)$_2$]TB. The efficiency of conversion of $Cp_2^*Ru^{(II)}$ (15 mM) to $[Cp_2^*Ru^{(IV)}(H)]^+$, in terms of the number of equivalents of acid required to achieve 100 % conversion, was monitored by ^{1}H NMR spectroscopy in the presence of [H(OEt$_2$)$_2$]TB. The raw NMR data as a function of increasing organic acid concentration are illustrated on the right and outlines the evolution of the signal corresponding to (A) the methyl group of $Cp_2^*Ru^{(II)}$ (blue circles, δ = 1.62 ppm), the methyl group of $[Cp_2^*Ru^{(IV)}(H)]^+$ (orange inverted triangles, δ = 1.85 ppm) and (B) the hydridic proton (green square, δ = –8.38 ppm). ^{1}H NMR spectra were obtained in CD_2Cl_2 using DCE (31.2 mM) as an internal standard, in the dark and under anaerobic conditions.

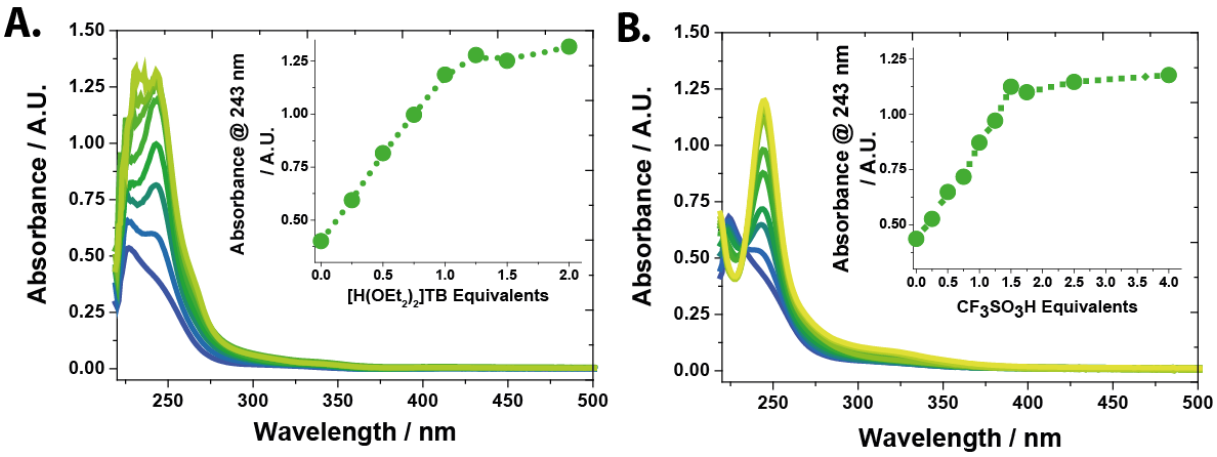

Figure S3. Metal hydride formation followed by UV/vis spectroscopy. The conversion of $Cp_2^*Ru^{(II)}$ (50 μM) to $[Cp_2^*Ru^{(IV)}(H)]^+$ was monitored by UV/vis spectroscopy in the dark in the presence of various concentration of **(A)** $[H(OEt_2)_2]TB$ and **(B)** CF_3SO_3H. Inset, the absorbance at 243 nm corresponding to the appearance of $[Cp_2^*Ru^{(IV)}(H)]^+$.

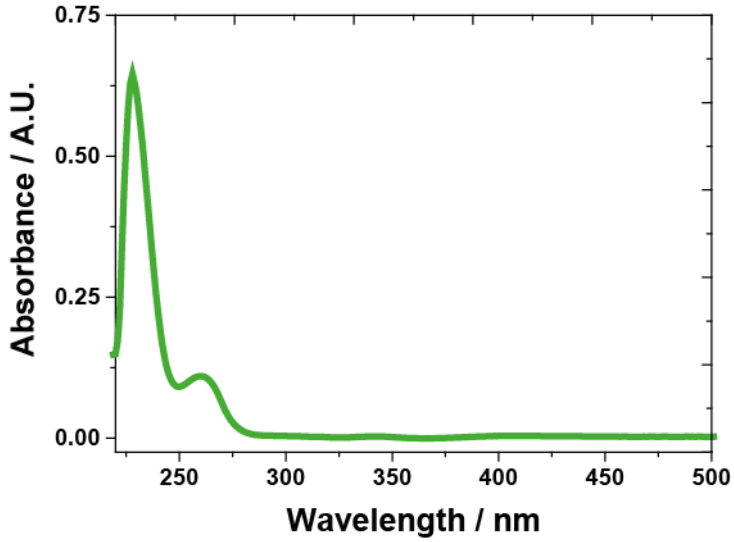

Figure S4. UV/vis spectrum of $H(OEt_2)_2]TB$ organic acid. UV/vis spectrum recorded for a solution of 80 μM $[H(OEt_2)_2]TB$ in DCE.

Section 3: Influence of coordinating solvent and of the electrolyte on the voltammetry of decamethylruthenocene in organic solvents, and spectroelectrochemical characterization of the $[Cp_2^*Ru^{(III)}]^+$ species.

Hashidzume *et al.* have speculated that complexation of $[Cp_2^*Ru^{(III)}]^+$ with acetonitrile (ACN) can drastically shift the $Ru^{(III)}/Ru^{(IV)}$ redox potential.[8] Complexation increases the ease of oxidation of the $Ru^{(III)}$ species to the extent that $[Cp_2^*Ru^{(III)}{\cdot}ACN]^+$ oxidises more easily than $Cp_2^*Ru^{(II)}$. Thus, $[Cp_2^*Ru^{(III)}{\cdot}ACN]^+$ species formed after the oxidation of $Cp_2^*Ru^{(II)}$ will be instantly oxidised to $[Cp_2^*Ru^{(IV)}{\cdot}ACN]^{2+}$ at the same potential. This gives rise to an apparent 2 e^- oxidation of $Cp_2^*Ru^{(II)}$. However, due to steric hindrances from the permethylated cyclopentadienyl rings, complexation with ACN is proposed to be an equilibrium reaction with the majority of the species non-complexed. Thus, the apparent observed electron transfer should be less than 2 on the forward (oxidising) sweep. This gives rise to a large first reduction peak on the reverse sweep, corresponding to the reduction of uncomplexed $[Cp_2^*Ru^{(III)}]^+$ to $Cp_2^*Ru^{(II)}$, and a much smaller second reduction peak, due to the reduction of the small amount of $[Cp_2^*Ru^{(IV)}{\cdot}ACN]^{2+}$ present to $[Cp_2^*Ru^{(III)}{\cdot}ACN]^+$. The latter complex will lose its ACN ligand and, as the electrode potential is already at a lower (more negative) value than the standard potential of the $Ru^{(II)}/Ru^{(III)}$ redox couple, $[Cp_2^*Ru^{(III)}]^+$ will be further reduced to $Cp_2^*Ru^{(II)}$ in an Electrochemical-Chemical-Electrochemical (ECE) mechanism.[8] Further studies would be beneficial to clarify this mechanism. For example, if the $Ru^{(III)}/Ru^{(IV)}$ redox potential is not in fact significantly shifted on complexation of $[Cp_2^*Ru^{(III)}]^+$ with ACN, then the small irreversible reduction wave at more negative potentials on the reverse sweep may alternatively be due to reduction of $[Cp_2^*Ru^{(III)}{\cdot}ACN]^+$. In this case the minor amount of $[Cp_2^*Ru^{(III)}{\cdot}ACN]^+$ formed may be more stable than the uncomplexed $[Cp_2^*Ru^{(III)}]^+$ species, shifting the $Ru^{(II)}/Ru^{(III)}$ redox potential for the former to lower potentials.

It is worth noting that, with the exception of extremely weakly coordinating anions such as TB^- and $B(C_6H_3(CF_3)_2)_4]^-$, coordination by many typical supporting electrolyte anions, such as Cl^-, ClO_4^-, BF_4^-, or PF_6^-, dramatically influences the electrochemistry of the less sterically hindered ruthenocene ($Cp_2Ru^{(II)}$) complex.[9] Ultimately this leads to the observation of irreversible 2 e^- oxidation of $Cp_2Ru^{(II)}$ by various proposed mechanisms (*i.e.*, rapid dimerization of $[Cp_2Ru^{(III)}]^+$ followed by disproportionation or, alternatively, disproportionation of $[Cp_2Ru^{(III)}]^+$ in the presence of even weakly coordinating ligands).

As discussed above and in the main text, it appears that $[Cp_2^*M^{(III)}]^+$ (M = Os or Ru) species can be stabilized by utilizing soft weakly complexing counter-anions and weakly coordinating solvents. In this work we utilized tetrakis(pentafluorophenyl) borate (TB^-) to

stabilize the $[Cp_2^*M^{(III)}]^+$ in DCE solution (a non-coordinating solvent) containing bis(triphenylphosphoranylidene)ammonium tetrakis(pentafluorophenyl) borate (BATB) supporting electrolyte, successfully preparing $[Cp_2^*Ru^{(III)}]$TB species by electrochemical oxidation of $Cp_2^*Ru^{(II)}$. The spectroscopic identification of the produced $[Cp_2*Ru^{(III)}]^+$ species was achieved by preparing $[Cp_2*Ru^{(III)}]$TB *via* oxidation of 6 mM $Cp_2*Ru^{(II)}$ in a solution of DCE containing BATB supporting electrolyte.

The solution was oxidized for 120 s at a series of applied potentials spaced at regular intervals between – 0.78 and 0.73 V (*vs.* $[Cp_2*Ru^{(III)}]^+/ Cp_2*Ru^{(II)}$ couple). The response at each applied potential was followed by UV/vis spectroscopy. As seen in Figure S5, a characteristic absorbance, with a maximum (λ_{max}) centered at 500 nm, appeared confirming the presence of $[Cp_2*Ru^{(III)}]$TB as an intermediate during the catalysis. On the time-scale of this experiment (120 s), all $Cp_2*Ru^{(II)}$ molecules present were converted to $[Cp_2*Ru^{(III)}]^+$. This was reflected in the observed plateau in absorbance at 500 nm and by a decrease of the current beyond this applied potential. Finally, the molar extinction coefficient of $[Cp_2*Ru^{(III)}]^+$ in DCE was determined using the Beer-Lambert Law as 0.960 $mM^{-1}\cdot cm^{-1}$, with an optical path length of 1 mm, and an absorbance of 0.576 at the end of the experiment that corresponds to 6 mM of $[Cp_2*Ru^{(III)}]^+$ generated by exhaustive electrolysis.

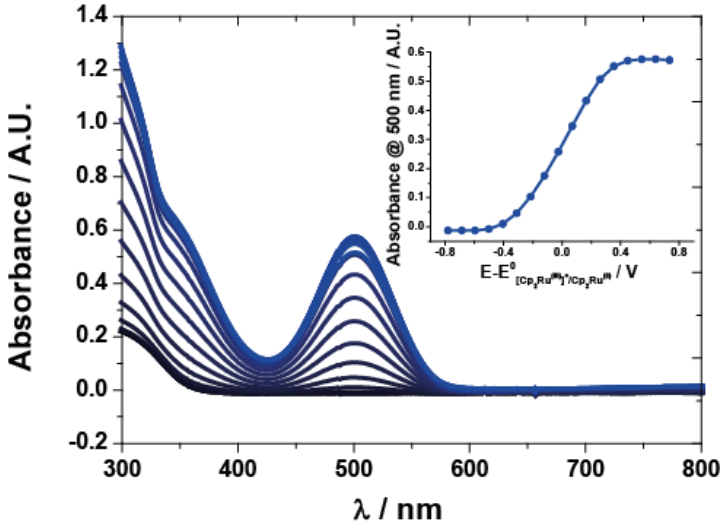

Figure S5. Spectroelectrochemical characterization of the generation of $[Cp_2*Ru^{(III)}]^+$ as a function of the applied potential. Oxidation of a 6 mM solution of $Cp_2*Ru^{(II)}$ in de-oxygenated DCE with 20 mM BATB as supporting electrolyte, was performed by applying various potentials at regular intervals between – 0.78 and 0.73 V (*vs.* $[Cp_2*Ru^{(III)}]^+/ Cp_2*Ru^{(II)}$ couple)for 120 s under anaerobic conditions. $[Cp_2*Ru^{(III)}]^+$ has a UV/vis absorbance maximum (λ_{max}) at 500 nm. Inset, the variation of absorbance at 500 nm plotted as a function of applied potential.

Section 4: In-depth electrochemical studies.

Cyclic voltammograms (CVs) were performed as an initial probe of the electrocatalytic activity of Cp_2*$Ru^{(II)}$ towards H_2 generation. Scans were recorded at a Fluorinated Tin Oxide (FTO) electrode in DCE, with tetrabutylammonium hexafluorophosphate ($TBAPF_6$) as the supporting electrolyte, under anaerobic conditions and at ambient temperature (the experimental set-up is shown in Figure S6).

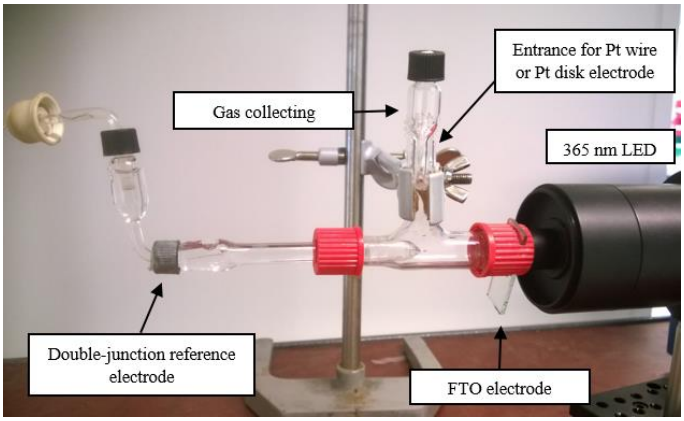

Figure S6: Cell used for photo-electrochemical measurments and collection of H_2 gas.

CVs of $Cp_2^*Ru^{(II)}$ in the absence of acid in Figure S7 clearly show an oxidation and a reduction peak for the $Ru^{(III)}/Ru^{(II)}$ redox process with a current linearly dependent on the square root of the scan rate. The formal redox potential of $Cp_2^*Ru^{(II)}$, $[E^{0\prime}_{[Cp_2Ru(III)]^+/Cp_2Ru(II)}]^{DCE}$, was determined as 0.75 V *versus* the aqueous standard hydrogen electrode (SHE). The latter is equivalent to 1.39 V *versus* the ferrocenium cation/ferrocene ($[Cp_2Fe^{(III)}]^+/Cp_2Fe^{(II)}$) redox couple (Figure S7). Experimentally, the potential was calibrated *versus* the formal reduction potential of Cp_2*$Fe^{(II)}$ in DCE on the standard hydrogen electrode (SHE) scale ($[E^{0\prime}_{[Cp_2Fe(III)]^+/Cp_2Fe(II)}]^{DCE}$ = 0.07 V *vs.* SHE).[6]

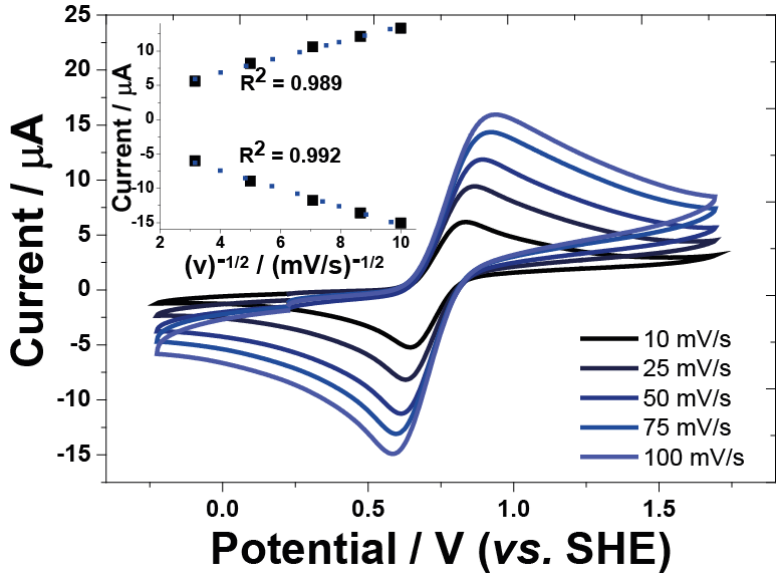

Figure S7: Cyclic voltammograms (CVs) of 1 mM Cp_2*$Ru^{(II)}$ at an FTO electrode at different scan rates. Cp_2*$Ru^{(II)}$ was dissolved in DCE containing 0.1 M $TBAPF_6$. Measurements were recorded under a N_2 atmosphere at ambient temperature using platinum wire as the counter electrode and a double-junction reference electrode as described above. CVs were calibrated *versus* the formal reduction potential of $Cp_2^*Fe^{(II)}$ in DCE on the SHE scale ($[E^{0\prime}_{[Cp_2*Fe(III)]^+/Cp_2*Fe(II)}]^{DCE}$ = 0.07 V *vs.* SHE). Thus, the formal redox potential of $Cp_2^*Ru^{(II)}$, $[E^{0\prime}_{[Cp_2Ru(III)]^+/Cp_2Ru(II)}]^{DCE}$ was determined as 0.75 V *versus* SHE. The peak currents increased linearly *versus* the square root of the scan rate for both the anodic and cathodic processes, characteristic of reversible electron transfer.

A series of further control electrochemical experiments were performed to fully characterize the behavior of each species in the electrochemical cell. Firstly, CVs of an electrochemical cell with only $[H(OEt_2)_2]TB$ and the supporting electrolyte present in the DCE solution did not shown any change in response under dark conditions and with LED illumination (Figure S8A). Subsequently, CVs in the absence of organic acid, with only Cp_2*$Ru^{(II)}$ and the supporting electrolyte present in the DCE solution, exhibited an oxidative catalytic wave under illumination (Figure S8B). The precise identification of this catalytic oxidation, possibly the catalytic oxidation of DCE by Cp_2*$Ru^{(II)}$ in the absence of organic protons, was outside the scope of this study. This side-reaction, while interesting, did not interfere with our interpretation of the CVs and controlled potential electrolysis (CPE) data obtained during the photo-electrocatalytic reduction of protons in the presence of Cp_2*$Ru^{(II)}$.

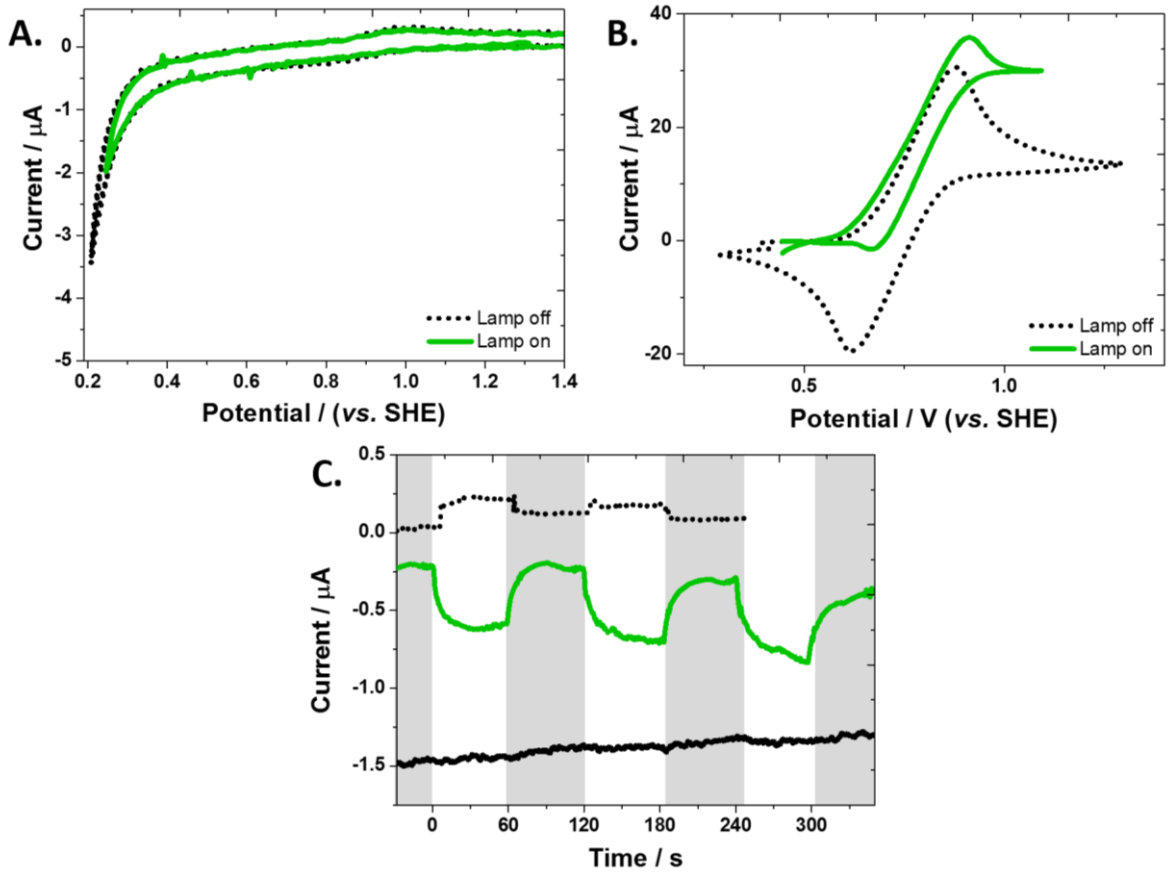

Figure S8: Control electrochemical experiments. All cyclic voltammograms (CVs) were obtained at 5 $mV \cdot s^{-1}$ at an FTO electrode in contact with a solution of DCE containing 0.1 M $TBAPF_6$ as supporting electrolyte. CVs were obtained under anaerobic conditions at ambient temperatures using platinum wire as the counter electrode and a double-junction reference electrode, as described above. Measurements were calibrated *versus* the formal reduction potential of $Cp_2^*Fe^{(II)}$ in DCE on the SHE scale ($[E^{0\prime}_{[Cp_2^*Fe(III)]^+/Cp_2^*Fe(II)}]^{DCE}$ = 0.07 V *vs.* SHE). **(A)** CVs of 4 mM $[H(OEt_2)_2]TB$ without (dark dot) and with (green line) illumination at λ = 365 nm. **(B)** CVs of 1 mM $Cp_2^*Ru^{(II)}$ without (dark dot) and with (green line) illumination at λ = 365 nm. **(C)** Chronoamperometry periodically turning the light off (grey) and on (white) with 1 mM $Cp_2^*Ru^{(II)}$ in solution at 0.50 V *vs.* SHE (dark dotted line), 1 mM $Cp_2^*Ru^{(II)}$ and 4 mM $[H(OEt_2)_2]TB$ in solution at 0.50 V *vs.* SHE (green line), and 4 mM $[H(OEt_2)_2]TB$ in solution at 0.35 V (dashed line).

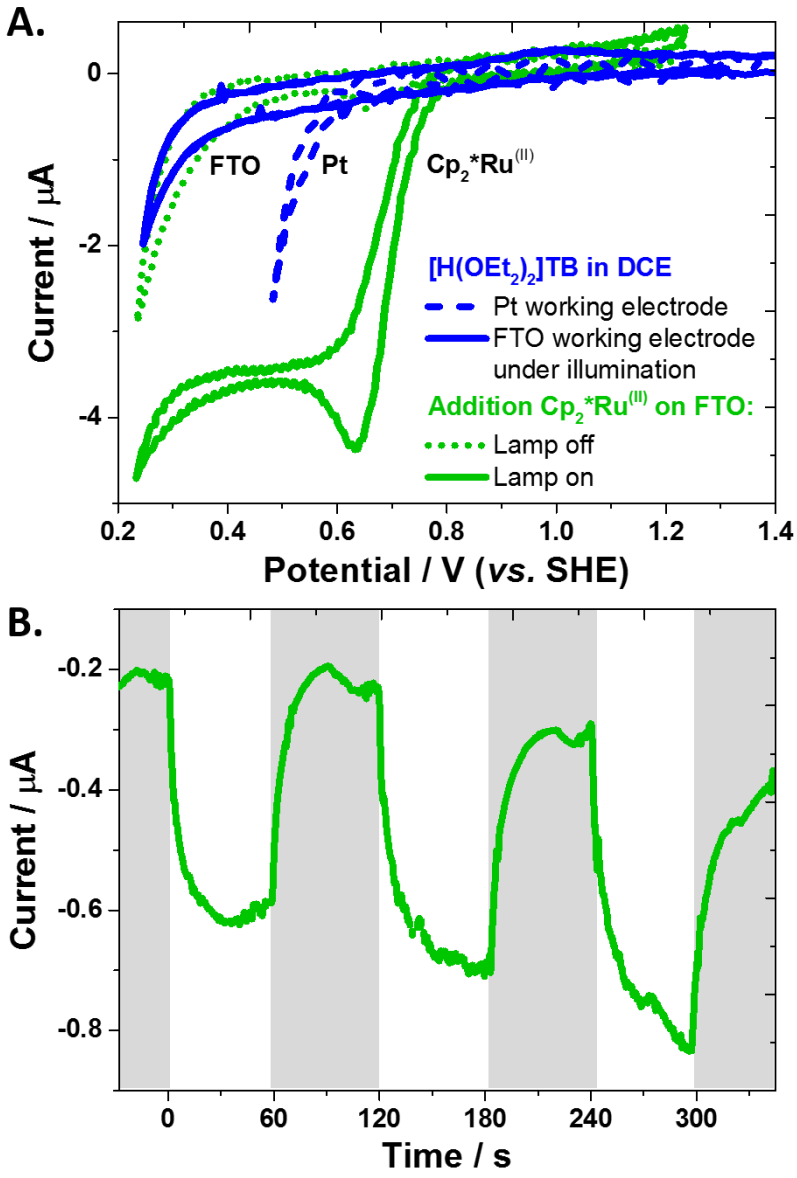

Figure S9: Full electrochemical measurements. (A) CV of 4 mM $[H(OEt_2)_2]TB$ in DCE with 0.1 M $TBAPF_6$ supporting electrolyte without (FTO – solid blue and Pt – dashed blue lines) or with 1 mM $Cp_2*Ru^{(II)}$ (green CVs with and without illumination). Scan rate 5 $mV \cdot s^{-1}$. Reduction of the photoproduct occurs at a potential more positive compare to the direct reduction of protons on Pt. The comparison with Pt highlights the more favorable regeneration of $Cp_2*Ru^{(II)}$ towards water splitting applications. (B) Zoom on the experiment in Figure S8(C), green line. A solution of 1 mM $Cp_2*Ru^{(II)}$ and 4 mM $[H(OEt_2)_2]TB$ in DCE with 0.1 M $TBAPF_6$ as supporting electrolyte on an FTO electrode at 0.50 V *vs.* SHE was subjected to controlled potential electrolysis with the LED illumination switched periodically on (white) and off (grey).

Section 5: Gas chromatographic and UV/vis spectroscopic analysis of the reaction products of controlled potential electrolysis.

The generation of H_2 in the presence of organic protons, $Cp_2^*Ru^{(II)}$ and light was definitively proven by photo-electrolysis at an applied potential of 0.50 V *vs.* SHE. The headspace of the electrochemical cell was monitored by gas chromatography and clearly showed the formation of H_2 (see Figure S10). The quantity of H_2 evolved was compared with that for a reaction running without electrochemical regeneration (also Figure S10).

Without regeneration, $Cp_2^*Ru^{(II)}$ acts as an electron donor capable of producing two equivalents of H_2 for each equivalent of $Cp_2^*Ru^{(II)}$ present in solution. One equivalent corresponds to the oxidation of the hydride. The second equivalent is due to the extraction of a proton from one of the methyl groups on the cyclopentadienyl rings. In other words, the permethylated cyclopentadienyl (Cp*) group is converted from (η^5-C_5Me_5) to a methylenecyclotetradienyl (η^5-$C_5Me_4CH_2$) ligand. This breakdown mechanism of $Cp_2^*Ru^{(II)}$ in the presence of light and an organic acid, but ***absence of regeneration***, is the subject of a detailed forthcoming publication form our group.[10]

The quantities of H_2 evolved without regeneration are in good, but not perfect, agreement with our forthcoming report studying the reaction mechanism of the photoproduction of H_2 with $Cp_2^*Ru^{(II)}$ in a single acidified organic phase.[10] Despite the caution taken to entirely seal the electrochemical cell, a small amount of H_2 permeated through the electrochemical cell. Indeed, because H_2 is a leaky small molecule, the quantification of the long term H_2 release from the electrode junction with an electrochemical cell is an issue for these kinds of measurements.[11] Nevertheless, a noticeable enhancement in H_2 production was observed when the potential was applied at the FTO electrode for 4 hours (see Figures S10 and S11) meaning the electro-regeneration occurred.

The color of the organic solution turned from colorless to pink during the reaction. Subsequent analysis by UV/vis spectroscopy revealed a characteristic absorbance band at 500 nm (see Figure S12), identified as the $[Cp_2^*Ru^{(III)}]^+$ species earlier in Figure S5. Additionally, a broad band appeared at a higher wavelength which indicated the decomposition of $[Cp_2^*Ru^{(III)}]^+$ was beginning to take place (Figure S12). After 6 hours without regeneration, decomposition of $[Cp_2^*Ru^{(III)}]^+$ occurred giving way to a series of ill-defined absorbance bands (Figure S12).

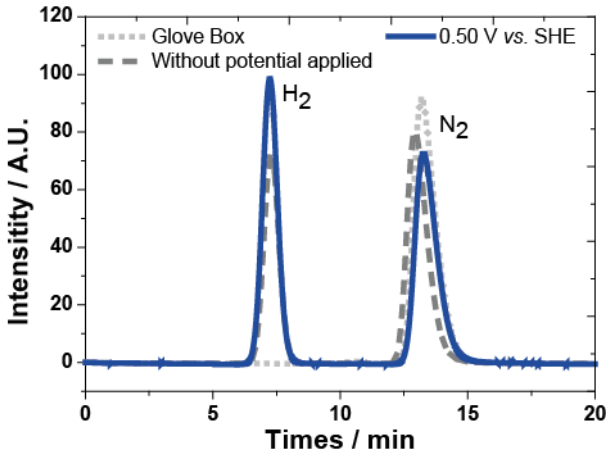

Figure S10: **Gas chromatogram of the photo-production of H_2 gas from a solution of 1 mM $Cp_2Ru^{(II)}$ with 6 mM $[H(OEt_2)_2]TB$ in DCE.** The solution was put in contact with an FTO electrode, stirred and illuminated overnight at λ = 365 nm using the LED during 10 hours. A potential of 0.50 V *vs.* SHE was applied at the FTO electrode during the first 4 hours. The electrochemical cell used is depicted in Figure S6 above, with a platinum wire counter electrode and a double-junction reference electrode. The headspace of the airtight cell was analysed after 10 hours (blue line). To compare, an identical experiment was performed without applying a potential (grey dash). A noticeable enhancement of the H_2 production was observed while the potential was applied. The atmosphere inside the gloves box was analysed as a control experiment for each reaction (grey dot). No hydrogen or oxygen were observed.

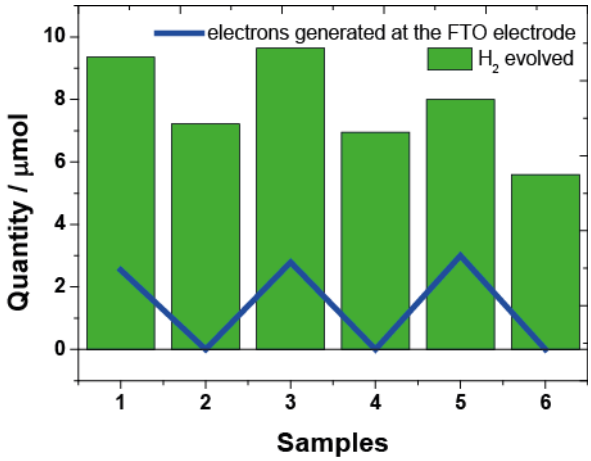

Figure S11. Comparison of H_2 production with or without electrochemical regeneration. A solution of 1 mM $Cp_2*Ru^{(II)}$ with 6 mM $[H(OEt_2)_2]TB$ was placed in the electrochemical cell presented in Figure S6 and illuminated for 10 hours under LED illumination. The head space of the cell was analysed (green bar). The result clearly shows the enhancement of the H_2

production while a potential of 0.50 V *vs.* SHE was applied (the quantity of electrons passing through the FTO electrode is signified by the blue line).

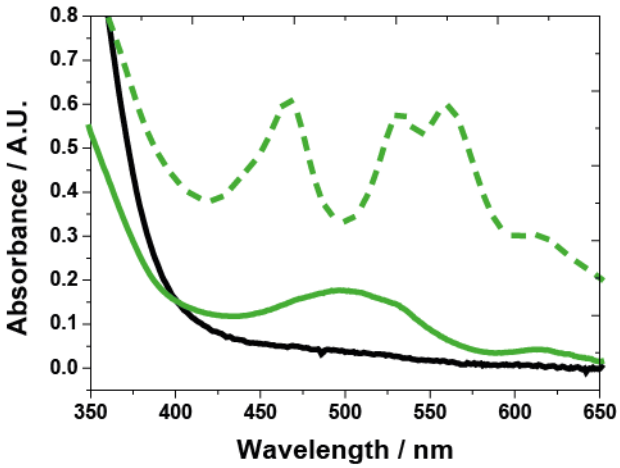

Figure S12: Uv/vis spectra of a solution containing 1 mM $Cp_2^*Ru^{(II)}$ and 4 mM $[H(OEt_2)_2]TB$ before the reaction (dark line) and during controlled potential electrolysis at 0.50 V *vs.* SHE under LED illumination (green line) and 6 hours after controlled potential electrolysis (green dash). A rise of absorbance at 500 nm is induced by the generation of $[Cp_2Ru^{(III)}]^+$ (characterized by spectroelectrochemistry in Figure S5).

Section 6: Quantum yield calculations.

The photon flux

The photon flux was calculated by measuring the LED power, which was adjusted to a desired value and measured using a Newport 918D-UV-OD3 assuming all photons had the same wavelength of 365 nm (5.45×10^{-19} Joule/photon). In this adjustment of the power we accounted for the irradiated area over the sample, as well as for the absorption of the reaction cell window and other minor losses in the setup.

The LED wavelength (λ) used was 365 nm; therefore the energy each photon carries is:

$$E_{photon} = (h \cdot c)/\lambda = 6.626 \times 10^{-34}\ (J \cdot s) \cdot 3 \times 10^{8}\ (m \cdot s^{-1}) / 365 \times 10^{-9}\ (m) \quad (S1)$$

$$E_{photon} = 5.45 \times 10^{-19}\ J / photon \quad (S2)$$

where h is Planck's constant and c is the speed of light.

The LED power was set to 11 mW, thus the photon flux (amount of photons per second) is given by:

$$\text{Photon flux} = \text{LED power}/E_{photon} \quad (S3)$$

$$= 11 \times 10^{-3}\ (J \cdot s^{-1}) / 5.45 \times 10^{-19}\ (J / photon)$$

$$= 2.0 \times 10^{16}\ photons \cdot s^{-1}$$

Calculating the Internal Quantum Yield (IQY)

The absorbance observed from the UV/vis spectra presented in Figure S13 at 500 nm was converted to concentration of $[Cp_2{*}Ru^{(III)}]^+$ by applying the Beer-Lambert law, $A = l\ \varepsilon\ c$, with l = 4.2 cm and ε = 0.960 mM · cm^{-1} (determined previously during the spectroelectrochemical experiment shown in Figure S5). The UV/vis spectra of the reference cell filled only with DCE was subtracted to the UV/vis spectra of $[Cp_2{*}Ru^{(III)}]^+$ obtained meaning that the QY obtained does not depend on the reflectance and transmittance of the cell. The length of the cell was selected in order to guarantee the absorption of the entirety of the incident light. The experiments were performed inside a glove box to avoid any O_2 contamination. A sample of the gas inside the gloves box was analysed by GC. No O_2 was observed.

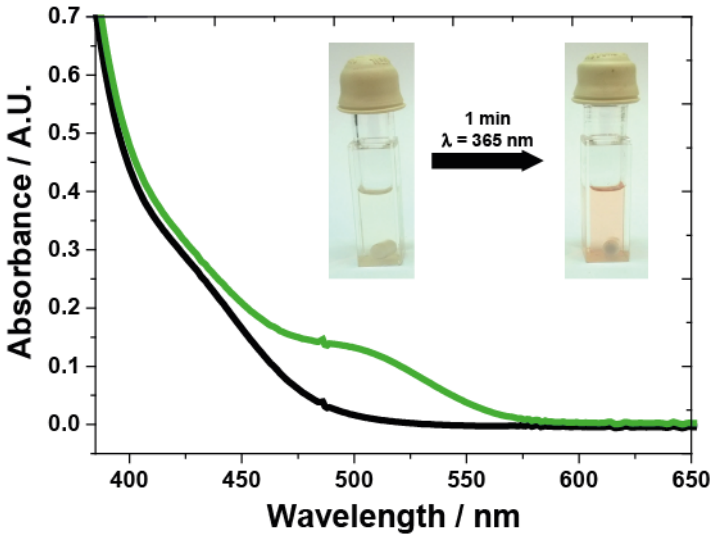

Figure S13: **Uv/vis spectra of a solution containing 2 mM Cp_2*$Ru^{(II)}$ and 8 mM [$H(OEt_2)_2$]TB** before the reaction (dark line) and after one minute of illumination with a 365 nm LED (green line). Generation of $[Cp_2Ru^{(III)}]^+$ under illumination induces to the rise of absorbance at 500 nm. The production of $[Cp_2Ru^{(III)}]^+$ was quantified using the extinction coefficient determined spectroelectrochemically in Figure S5 by applying the Beer-Lambert law. The quantified $[Cp_2Ru^{(III)}]^+$ was then used to calculate the internal quantum yield of the photo-reaction.

At 11 mW of power we obtained a concentration of 32.8 μM $[Cp_2Ru^{(III)}]^+$ for 15 mL, meaning 3.0×10^{17} molecules were produced.

Next we calculated the production rate as the number of $[Cp_2Ru^{(III)}]^+$ molecules per second: 3.0×10^{17} / 60 s = 4.9×10^{15} s^{-1}.

Thus, the internal quantum yield of the sample is defined as IQY = n $[Cp_2{*}Ru^{(III)}]^+$ / n_{hv}

IQY = 100 % · (4.9×10^{15} / 2.0×10^{16}) = 24.7 %.

Calculating the theoretical External Quantum Yield (EQY)

The transmittance observed from the transmittance spectrum of the FTO glass electrode presented in Figure S14 was used to calculate the EQY.

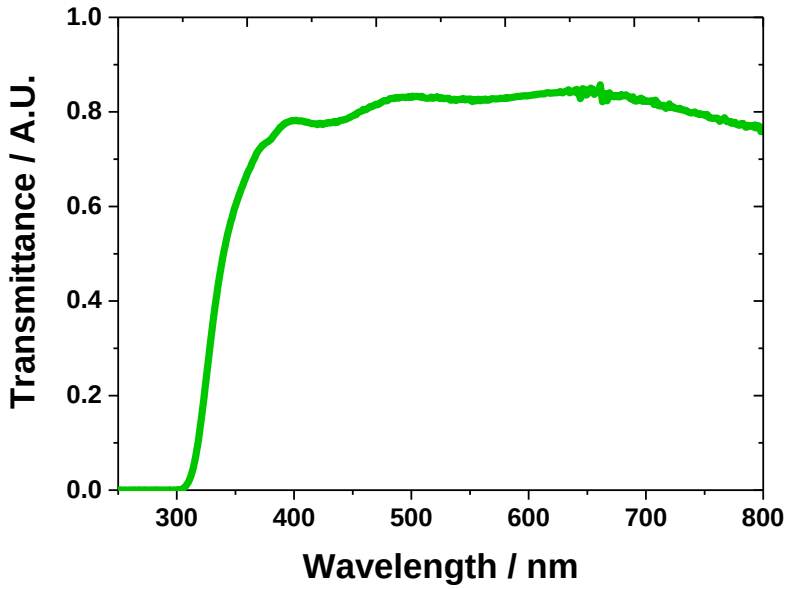

Figure S14: **Transmittance spectrum of FTO glass electrode.** Air was taken as blank. A transmittance of 69.7 % was observed at 365 nm.

Thus, the maximum production rate expected as the number of $[Cp_2Ru^{(III)}]^+$ molecules per second when the cell is illuminated through the FTO electrode is given by:

$4.9 \times 10^{15} \cdot s^{-1} \times 0.697 = 3.4 \times 10^{15}$ photons$\cdot s^{-1}$

Therefore, the maximum EQY expected was directly obtained from the new production rate:

$EQY = 100\ \% \cdot (3.4 \times 10^{15} / 2.0 \times 10^{16}) = 17.0\ \%$

Section 7: The photo-excited properties of $[Cp_2^*Ru^{(IV)}(H)]^+$.

Wavelength dependence of the excitation of $[Cp_2^*Ru^{(IV)}(H)]^+$

The features of the UV/vis spectrum of $[Cp_2^*Ru^{(IV)}(H)]^+$ were discussed earlier in Section 2 during titration of $Cp_2*Ru^{(II)}$ by the strong organic acids $[H(OEt_2)_2]TB$ and CF_3SO_3H. A study was performed to analyse the IQY of the photo-reaction as a function of the wavelength of illumination. A maximum yield of 37 % was achieved at 243 nm corresponding to the maximum absorbance band of $[Cp_2^*Ru^{(IV)}(H)]^+$. This result confirms that the mechanism involves the excitation of the hydride in the first stage of the reaction. The yield was divided by three at 229 nm and also decreased in the near UV region (300 nm < λ < 400 nm). No H_2 or $[Cp2*Ru^{(III)}]^+$ production were observed at 455 nm. Although care was taken to ensure good illumination of the sample, the quantum yield obtained at 365 nm with the laser (*ca.* 7 %) is smaller than the one determined with an LED source (*ca.* 25 %). This can result from the different conditions of the experiment as well as the polarized laser light used. Indeed, molecules which are oriented such that their transition dipole moment is parallel to the *k* vector of the incident photons (and perpendicular to the plane of the polarization vectors) were not excited.[12] Herein, the cell was prepared inside a glove box and, then, taken out to be illuminated with the laser light. Thus, the cell was slightly contaminated by atmospheric O_2 (visible by GC). Consequently, a higher quantity of $[Cp_2*Ru^{(III)}]^+$ was observed compare to the H_2 production method of quantification of the IQY due to the reduction of O_2. Indeed, this reaction is thermodynamically more favourable than the reduction of a proton and the two reactions compete.[13] It was observed, as thermodynamically expected, that as the wavelength shifted to the UV (*i.e.* higher energy), proton reduction became more favourable in comparison to O_2 reduction.

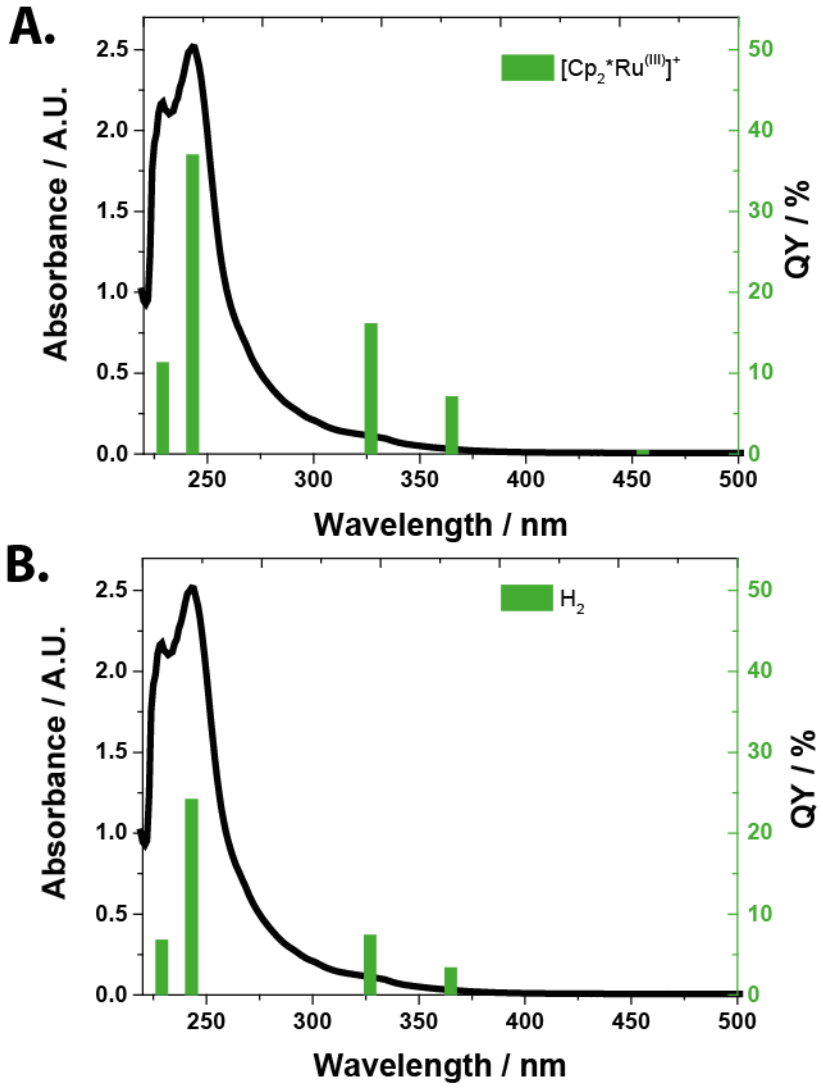

Figure S15: **Wavelength dependence of the HER by Cp_2*$Ru^{(II)}$ as a function of the wavelength excitation.** A solution of 6 mM Cp_2*$Ru^{(II)}$ with 12 mM $[H(OEt_2)_2]TB$ was prepared inside a glove box, sealed with a septum and, then, illuminated outside the glove box under stirring conditions for 10 min. at various wavelengths. The power was modulated in order to keep the number of emitted photon constant and equal to 1.8 μmol. The EQY was obtained by determining the quantity of **(A)** $[Cp_2Ru^{(III)}]^+$ produced by UV/visible spectroscopy and **(B)** H_2 produced by GC. Results are compared with the $[Cp_2{}^*Ru^{(IV)}(H)]^+$ spectrum (black line).

Computed absorption spectrum of $Cp_2^*Ru^{(IV)}(H)]^+$.

The absorption spectrum of $[Cp_2^*Ru^{(IV)}(H)]^+$ was computed at the TD-ωB97X-D/def2-TZVP level[14] using the first 20 singlets excitation and a SMD solvation model[15] for 1,2-dichloroethane (ε=10.125). The geometry was optimized in the gas phase at the M06/def2-TZVP level.[16] The natural transition orbitals[17] and electron density difference are given below for the most intense absorption band (λ=227nm). The excited state density was obtained by adding to the converged DFT wavefunction the necessary Z-vector contribution derived from a coupled-perturbed Kohn-Sham (CPKS) calculation for state *N*.[18] All computations were performed using Gaussian'09.[19]

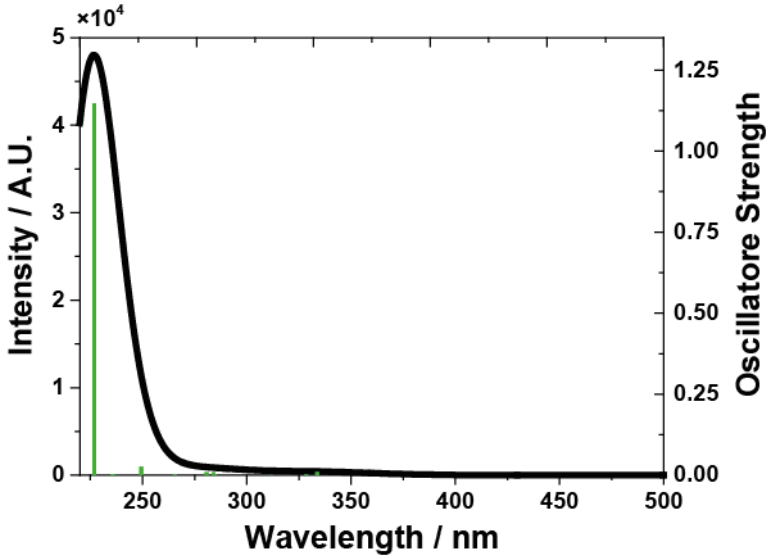

Figure S16: The absorption spectrum of $[Cp_2^*Ru^{(IV)}(H)]^+$ computed at the TD-ωB97X-D/def2-TZVP level using a SMD solvation model for 1,2-dichloroethane (ε=10.125).

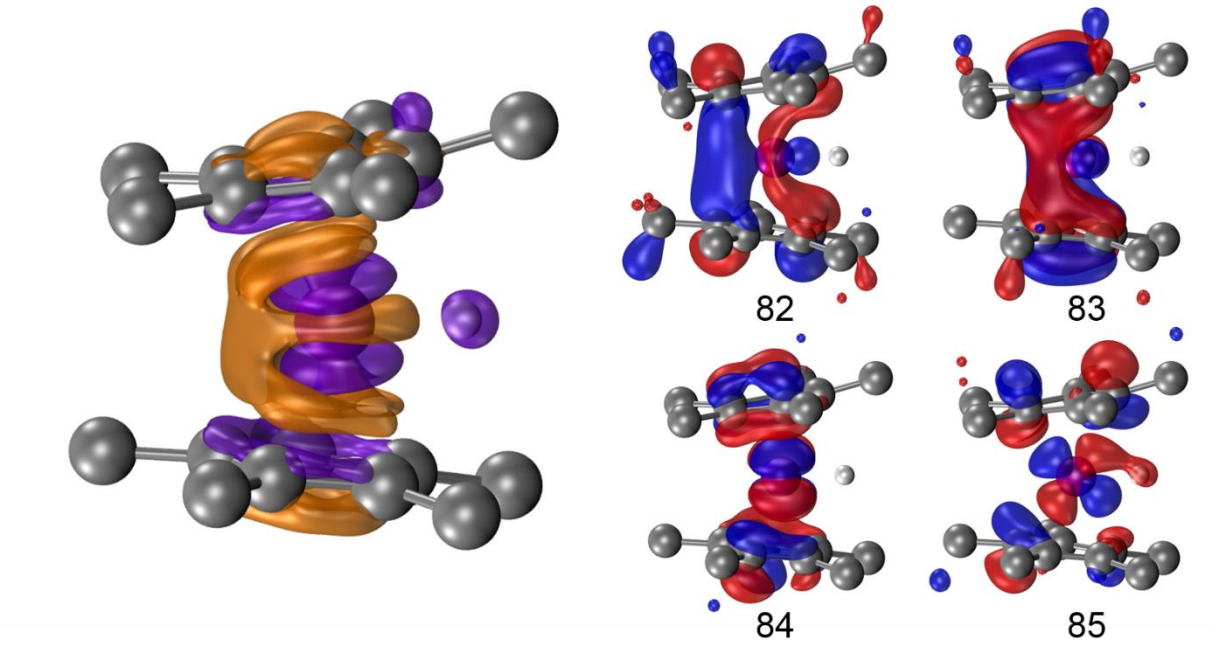

Figure S17: Density difference (excited – ground state) of $[Cp_2^*Ru^{(IV)}(H)]^+$, isodensities = +0.002(violet) / -0.002(orange) (left). Natural Transition Orbitals participating to the λ=227nm excitation (right). Densities and orbitals computed at the ωB97X-D/def2-TZP level using a SMD solvation model for 1,2-dichloroethane (ε=10.125) on gas phase M06/def2-TZVP optimized geometry.

Table S1: Excitation energies, oscillator strengths and natural transition orbitals contributions for the λ=227nm excitation of [Cp2*Ru(IV)(H)]+, computed at the ωB97XD/def2-TZP level using a SMD solvation model for dichloroethane (ε=10.125) on gas phase ground state M06/def2-TZVP optimized geometry.

system	λ [nm]	*f*	transition	contribution
[Cp2*Ru(IV)(H)]+	227	1.1466	83 → 84	58%
			82 → 85	38%

References:

[1] D. J. Fermin, H. D. Duong, Z. Ding, P.-F. Brevet, H. H. Girault, *Physical Chemistry Chemical Physics* **1999**, *1*, 1461-1467.

[2] E. S. Stoyanov, K.-C. Kim, C. A. Reed, *Journal of the American Chemical Society* **2006**, *128*, 8500-8508.

[3] C. A. Reed, K.-C. Kim, E. S. Stoyanov, D. Stasko, F. S. Tham, L. J. Mueller, P. D. W. Boyd, *Journal of the American Chemical Society* **2003**, *125*, 1796-1804.

[4] aC. A. Reed, *Accounts of Chemical Research* **2010**, *43*, 121-128; bC. A. Reed, *Accounts of Chemical Research* **2013**, *46*, 2567-2575; cP. Jutzi, C. Müller, A. Stammler, H.-G. Stammler, *Organometallics* **2000**, *19*, 1442-1444.

[5] G. R. Fulmer, A. J. M. Miller, N. H. Sherden, H. E. Gottlieb, A. Nudelman, B. M. Stoltz, J. E. Bercaw, K. I. Goldberg, *Organometallics* **2010**, *29*, 2176-2179.

[6] N. Eugster, D. J. Fermín, H. H. Girault, *The Journal of Physical Chemistry B* **2002**, *106*, 3428-3433.

[7] aM. O. Albers, D. C. Liles, D. J. Robinson, A. Shaver, E. Singleton, M. B. Wiege, J. C. A. Boeyens, D. C. Levendis, *Organometallics* **1986**, *5*, 2321-2327; bA. A. Kamyshova, A. Z. Kreindlin, M. I. Rybinskaya, P. V. Petrovskii, *Russ Chem Bull* **1999**, *48*, 581-585.

[8] K. Hashidzume, H. Tobita, H. Ogino, *Organometallics* **1995**, *14*, 1187-1194.

[9] aJ. C. Swarts, A. Nafady, J. H. Roudebush, S. Trupia, W. E. Geiger, *Inorganic Chemistry* **2009**, *48*, 2156-2165; bS. Trupia, A. Nafady, W. E. Geiger, *Inorganic Chemistry* **2003**, *42*, 5480-5482; cM. G. Hill, W. M. Lamanna, K. R. Mann, *Inorganic Chemistry* **1991**, *30*, 4687-4690.

[10] aL. Rivier, T. J. Stockmann, M. A. Méndez, M. D. Scanlon, P. Peljo, M. Opallo, H. H. Girault, *The Journal of Physical Chemistry C* **2015**, *119*, 25761-25769; bL. Rivier, L. Vannay, M. Mendez, P. Peljo, H. Vrubel, C. Corminboeuf, M. D. Scanlon, H. H. Girault, **2016**.

[11] P. Adams, A. Bengaouer, B. Cariteau, V. Molkov, A. G. Venetsanos, *International Journal of Hydrogen Energy* **2011**, *36*, 2742-2749.

[12] C. Fichtner, M. van Gastel, W. Lubitz, *Physical Chemistry Chemical Physics* **2003**, *5*, 5507-5513.

[13] aI. Hatay, B. Su, F. Li, M. A. Méndez, T. Khoury, C. P. Gros, J.-M. Barbe, M. Ersoz, Z. Samec, H. H. Girault, *Journal of the American Chemical Society* **2009**, *131*, 13453-13459; bI. Hatay, B. Su, F. Li, R. Partovi-Nia, H. Vrubel, X. Hu, M. Ersoz, H. H. Girault, *Angewandte Chemie International Edition* **2009**, *48*, 5139-5142.

[14] aJ.-D. Chai, M. Head-Gordon, *Physical Chemistry Chemical Physics* **2008**, *10*, 6615-6620; bF. Weigend, R. Ahlrichs, *Physical Chemistry Chemical Physics* **2005**, *7*, 3297-3305.

[15] A. V. Marenich, C. J. Cramer, D. G. Truhlar, *The Journal of Physical Chemistry B* **2009**, *113*, 6378-6396.

[16] Y. Zhao, D. Truhlar, *Theor Chem Account* **2008**, *120*, 215-241.

[17] R. L. Martin, *J. Chem. Phys.* **2003**, *118*, 4775-4777.

[18] aK. B. Wiberg, C. M. Hadad, J. B. Foresman, W. A. Chupka, *J. Phys. Chem.* **1992**, *96*, 10756-10768; bN. C. Handy, H. F. Schaefer, *J. Chem. Phys.* **1984**, *81*, 5031-5033.

[19] M. J. Frisch, G. W. Trucks, H. B. Schlegel, G. E. Scuseria, M. A. Robb, J. R. Cheeseman, G. Scalmani, V. Barone, B. Mennucci, G. A. Petersson, H. Nakatsuji, M. Caricato, X. Li, H. P. Hratchian, A. F. Izmaylov, J. Bloino, G. Zheng, J. L. Sonnenberg, M. Hada, M. Ehara, K. Toyota, R. Fukuda, J. Hasegawa, M. Ishida, T. Nakajima, Y. Honda, O. Kitao, H. Nakai, T. Vreven, J. A. Montgomery Jr., J. E. Peralta, F. Ogliaro, M. J. Bearpark, J. Heyd, E. N. Brothers, K. N. Kudin, V. N. Staroverov, R. Kobayashi, J. Normand, K. Raghavachari, A. P. Rendell, J. C. Burant, S. S. Iyengar, J. Tomasi, M. Cossi, N. Rega, N. J. Millam, M. Klene, J. E. Knox, J. B. Cross, V. Bakken, C. Adamo, J. Jaramillo, R. Gomperts, R. E. Stratmann, O. Yazyev, A. J. Austin, R. Cammi, C. Pomelli, J. W. Ochterski, R. L. Martin, K. Morokuma, V. G. Zakrzewski, G. A. Voth, P. Salvador, J. J. Dannenberg, S. Dapprich, A. D. Daniels, Ö. Farkas, J. B. Foresman, J. V. Ortiz, J. Cioslowski, D. J. Fox, Gaussian, Inc., Wallingford, CT, USA, **2009**.